



Cite this: *RSC Adv.*, 2023, 13, 23829

Development of robust noble-metal free lanthanum, neodymium doped $\text{Li}_{1.05}\text{Ni}_{0.5}\text{Mn}_{1.5}\text{O}_4$ as a bifunctional electrocatalyst for electrochemical water splitting†

Kayalvizhi Rajagopal,^a Murugavel Kathiresan,^b Arulmozhi Rajaram,^a Abirami Natarajan ^{*a} and Kumaresan Natesan^c

Catalysts for oxygen evolution reaction (OER) and hydrogen evolution reaction (HER) are at the heart of water oxidation reactions. Despite continuous efforts, the development of OER/HER electrocatalysts with high activity at low cost remains a big challenge. Herein, we report a composite material consisting of $\text{Li}_{1.05}\text{Ni}_{0.5}\text{Mn}_{1.5}\text{O}_4$, $\text{Li}_{1.05}\text{Ni}_{0.5}\text{La}_{0.10}\text{Mn}_{1.40}\text{O}_4$, and $\text{Li}_{1.05}\text{Ni}_{0.5}\text{Nd}_{0.10}\text{Mn}_{1.40}\text{O}_4$ as a bifunctional electrocatalyst for OER and HER applications. Though the catalyst has a modest activity for HER, it exhibits high OER activity thereby making it a better nonprecious electrocatalyst for both OER and HER. The catalytic activity arises from the synergetic effects between LNM-La and LNM-Nd by a facile route that shows excellent and durable bifunctional catalytic activity for OER and HER in the alkaline medium developed. The LNM, LNM-La, and LNM-Nd displayed current densities of 2.17 V, 1.68 V, and 1.93 V vs. RHE at 10 mA cm^{-2} respectively. The Tafel slope values obtained for LNM, LNM-La, and LNM-Nd are about 419 mV dec^{-1} , 118 mV dec^{-1} , and 378 mV dec^{-1} respectively. These results indicate the superior electrocatalytic activity of LNM-La with facile OER kinetics.

Received 6th July 2023

Accepted 29th July 2023

DOI: 10.1039/d3ra04495e

rsc.li/rsc-advances

1. Introduction

The usage of fossil fuels, radioactive waste from the nuclear power plant, and the requirement for vast lakes and areas for wind and hydroelectric power generation all contribute to several problems with energy production worldwide. Researchers are therefore interested in creating alternative forms of energy to counteract rising environmental deterioration and the world's need for energy from traditional and unsustainable sources. Alternative secondary energy carriers available to reduce pollution and energy consumption include hydrogen, many kinds of biomass, solar, and nuclear energy.¹ Among the secondary energy carriers, hydrogen is a potential and transcendent energy source with great energy conversion efficiency and compatibility with the environment. Furthermore, the water electrolyzer and vapor reforming technologies are the most conventionally used methods for producing

hydrogen. The primary disadvantages of the vapor reforming technology are significant costs and global warming gas emissions during the hydrogen manufacturing process. To overcome these limitations, the water electrolyzer technique offers a simple and low-cost way to remove hydrogen from water.² Furthermore, water is a great source of hydrogen ions, which an electrolyzer can divide into hydrogen and oxygen. Water splitting by electrolysis is an appealing approach for extracting hydrogen and storing the energy as chemical energy *via* the oxygen evolution process and the hydrogen evolution reaction. Hydrogen is a potentially perfect energy source because of its remarkable energy density, high energy conversion efficiency, and conservation of nature.³ It is generally agreed that the most cost-effective method for producing renewable hydrogen involves the splitting of water into hydrogen and oxygen gas using novel high-voltage material.

Peng *et al.* demonstrated that substituting ions at the Mn site in LNM increases cathode cycle performance while decreasing the capacity with an increase in doping loading. The addition of Nd and La in $\text{Li}_{1.05}\text{Ni}_{0.5}\text{Mn}_{1.5}\text{O}_4$ might substantially increase reversible capacity.⁴ La and Nd in $\text{Li}_{1.05}\text{Ni}_{0.5}\text{La}_{0.10}\text{Mn}_{1.40}\text{O}_4$ and $\text{Li}_{1.05}\text{Ni}_{0.5}\text{Nd}_{0.10}\text{Mn}_{1.40}\text{O}_4$ respectively had the impact of forming lattice doping, reducing the crystal size to the nanoscale, increasing conductivity, and enhancing the rate of lithium-ion diffusion. The findings demonstrate that doping of rare earth elements is a viable strategy for enhancing the electrochemical

^aDepartment of Chemistry, Faculty of Engineering and Technology, SRM Institute of Science and Technology, Kattankulathur, Tamil Nadu-603203, India. E-mail: abiramin@srmist.edu.in; Tel: +91 9941223928

^bElectro Organic & Materials Electrochemistry Division, CSIR – Central Electrochemical Research Institute, Karaikudi, Tamil Nadu-630003, India

^cDepartment of Physics, SSN Research Centre, Sri Sivasubramaniya Nadar College of Engineering, Chennai, 603110, Tamil Nadu, India

† Electronic supplementary information (ESI) available. See DOI: <https://doi.org/10.1039/d3ra04495e>



characteristics of an electrocatalyst for water splitting. To develop a hydrogen-based economy, an electrolytic water oxidation process for the generation of oxygen and hydrogen *via* OER and HER may be utilized in a sustainable manner.⁵ OER is characterized by its slow kinetics, which consists of a multistep proton-coupled electron transfer at a thermodynamic potential of 1.23 V. $\text{Li}_{1.05}\text{Ni}_{0.5}\text{Mn}_{1.5}\text{O}_4$, $\text{Li}_{1.05}\text{Ni}_{0.5}\text{La}_{0.10}\text{Mn}_{1.40}\text{O}_4$, and $\text{Li}_{1.05}\text{Ni}_{0.5}\text{Nd}_{0.10}\text{Mn}_{1.40}\text{O}_4$ as bifunctional electrocatalyst is suitable for HER and both are stable in acid and alkaline conditions. Furthermore, the arrangement of Ni and Mn inside the spinel structure is a significant factor in determining the electrochemical characteristics of the compounds that have been synthesized. Due to the presence of Mn^{3+} ions, non-stoichiometric spinel with a disordered arrangement of Ni/Mn (corresponding space group $Fd\bar{3}m$) that has greater electrical conductivity and lithium diffusivity. During long-term charge and discharging, the ordered phase $\text{LiNi}_{0.5}\text{Mn}_{1.5}\text{O}_4$ with space group $P4_332$ has less lattice distortion and greater electrochemical stability than the $Fd\bar{3}m$ disordered phase.⁶ It was found that by manipulating the concentration of Mn^{3+} in the preparation process, it was able to vary the ratio of two spinel phases that were present in the material. The presence of two different crystallographic structures at the same time, $Fd\bar{3}m$ and $P4_332$, is one factor that leads to the excellent integrated electrochemical performance. On the other hand, the uneven distribution of Mn^{3+} on the surface speeds up the dissolution of Mn(II) , which in turn causes the active material's capacity to gradually decrease. In this work, we report the use of $\text{Li}_{1.05}\text{Ni}_{0.5}\text{Mn}_{1.5}\text{O}_4$, $\text{Li}_{1.05}\text{Ni}_{0.5}\text{La}_{0.10}\text{Mn}_{1.40}\text{O}_4$, and $\text{Li}_{1.05}\text{Ni}_{0.5}\text{Nd}_{0.10}\text{Mn}_{1.40}\text{O}_4$ as bifunctional electrocatalysts for water splitting for the first time. The as-prepared samples were analyzed using High-resolution scanning electron microscopy (HRSEM), transition electron microscopy (TEM), selected area electron diffraction (SAED), etching X-ray photoelectron spectroscopy (XPS), OER, and HER. This was done to identify the structural integrity and electrochemical features of the samples.

2. Materials and synthesis method

2.1 Materials

Lithium hydroxide monohydrate, nickel nitrate hexahydrate, manganese carbonate, lanthanum oxide, neodymium(III)oxide, and ethanol were purchased from Aldrich chemicals. For all the studies in this research, deionized water that has been purified by the Millipore Milli-Q system was employed. No additional purification was necessary because all the reagents were of analytical grade. The synthesis of $\text{Li}_{1.05}\text{Ni}_{0.5}\text{Mn}_{1.5}\text{O}_4$, $\text{Li}_{1.05}\text{Ni}_{0.5}\text{La}_{0.10}\text{Mn}_{1.40}\text{O}_4$, and $\text{Li}_{1.05}\text{Ni}_{0.5}\text{Nd}_{0.10}\text{Mn}_{1.40}\text{O}_4$ is described in the ESI (Fig. S1–S3†).

3. Results and discussion

3.1 Structure and morphology

X-ray diffraction was used to validate the phase purity of as synthesized $\text{Li}_{1.05}\text{Ni}_{0.5}\text{Mn}_{1.5}\text{O}_4$, $\text{Li}_{1.05}\text{Ni}_{0.5}\text{Nd}_{0.10}\text{Mn}_{1.40}\text{O}_4$, and $\text{Li}_{1.05}\text{Ni}_{0.5}\text{La}_{0.10}\text{Mn}_{1.40}\text{O}_4$. Fig. 1a shows the XRD pattern of $\text{Li}_{1.05}\text{Ni}_{0.5}\text{Mn}_{1.5}\text{O}_4$, the peaks at 19.28° , 29.07° , 33.60° , 36.87° ,

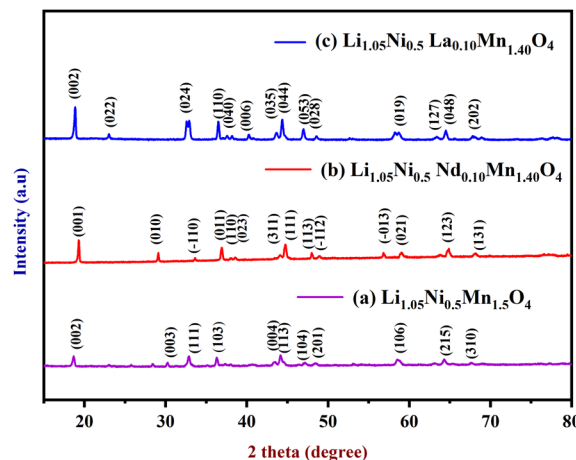


Fig. 1 XRD spectra of (a) $\text{Li}_{1.05}\text{Ni}_{0.5}\text{Mn}_{1.5}\text{O}_4$, (b) $\text{Li}_{1.05}\text{Ni}_{0.5}\text{Nd}_{0.10}\text{Mn}_{1.40}\text{O}_4$, and (c) $\text{Li}_{1.05}\text{Ni}_{0.5}\text{La}_{0.10}\text{Mn}_{1.40}\text{O}_4$.

38.55° , 44.07° , 44.71° , 47.98° , 64.76° , 74.63° , and 77.0° are ascribed to the crystal planes of (002), (003), (111), (103), (004), (113), (104), (201), (106), (215) and (310) respectively. Sharp diffraction peaks could be seen in the XRD pattern of $\text{Li}_{1.05}\text{Ni}_{0.5}\text{Mn}_{1.5}\text{O}_4$, suggesting the high degree of crystallinity of the sample.⁷ Without the presence of any impurity phase, all peaks may be properly indexed to the spinel structure. The diffraction peaks in the samples are sharp and the half-peak width is small, indicating that they have a high degree of crystallinity. The results show that the spinel structure was effectively preserved and that no impurity phases such as Ni–O and $\text{Li}_x\text{Ni}_{1-x}\text{O}$ were present. Depending on the ordering of transition metal cations, the structures are classified as face-centered spinel ($Fd\bar{3}m$) or primitive simple cubic crystal ($P4_332$). The transition metals Ni^{2+} and Mn^{4+} occupy the 4a and 12d lattice locations in the $P4_332$ space group, respectively. The oxygen ions are in places 24e and 8c, whereas the lithium ions are in position 8c. Lithium ions occupy the tetrahedral 8a sites in the $Fd\bar{3}m$ space group, while transition metal elements occupy the 16d octahedral sites.⁸ Fig. 1b shows the diffraction peaks coming from the spinel phase of the $\text{Li}_{1.05}\text{Ni}_{0.5}\text{Nd}_{0.10}\text{Mn}_{1.40}\text{O}_4$ which indicates a high degree of crystallinity because of the sharpness of the peaks. The peaks found at 18.64° , 25.76° , 32.83° , 35.13° , 36.28° , 37.28° , 40.64° , 44.16° , 47.10° , 48.42° , 58.59° , 60.29° , 68.98° , and 76.04° are attributed to the crystal planes of (001), (010), (–110), (011), (110), (023), (311), (111), (113), (–112), (–013), (021), (123) and (131) respectively. All the detected peaks may be attributed to spinel structure. There is no evidence of an impurity phase. In the inset of Fig. 1b, superstructure reflections (011), (110), (023), (311), (111), and (113), were seen; and these extra peaks show that the synthesized sample has a space group of $P4_332$ with Ni and Mn ions ordered in the locations of octahedral. The findings of XRD analysis show that Nd^{3+} has been evenly distributed on the bare material. Nd-doping will also enhance the lithium diffusion kinetics theory, the interrupted lithium migration pathway, the crystal's counterbalanced structure, and the widening of the lattice gap. Nd has a smaller ionic radius than La but a larger radius than Li^+ . Replacement of Nd^{3+} can



result in an enhanced A-site unorganized phase, resulting in a slightly enhanced conductivity of Li-ion, $1.26 \times 10^{-3} \text{ S cm}^{-1}$. Nd-doped cathode materials provide superior electrochemical efficiency in terms of cycle retention, voltage decay, and electrochemical impedance.⁹ The XRD patterns of $\text{Li}_{1.05}\text{Ni}_{0.5}\text{La}_{0.10}\text{Mn}_{1.40}\text{O}_4$ is shown in Fig. 1c, the peaks found at 18.68° , 22.94° , 32.45° , 36.34° , 37.75° , 40.37° , 44.16° , 46.81° , 52.59° , 58.45° , 63.13° , 64.22° , 68.31° , and 76.07° are endorsed to the crystal plane of (020), (022), (024), (110), (040), (006), (035), (044), (053), (028), (019), (127), (048), and (202) respectively. Sharp peaks and intensity can be well indexed to the spinel organized $\text{Li}_{1.05}\text{Ni}_{0.5}\text{La}_{0.10}\text{Mn}_{1.40}\text{O}_4$ with $Fd\bar{3}m$ phase P_{432} phase. The negative shift of the (024) crystal plane correlates to the expansion of the *c*-axis value, which signifies an increase in the interlaminar distance of the Li-layer. La^{3+} filled a portion of the octahedral sites, and La–O has greater bonding energy to strengthen the accumulation of oxygen and enlarge the Li-layer space, allowing for the insertion/extraction of Li^+ . The (220) peak is absent from the XRD pattern of $\text{Li}_{1.05}\text{Ni}_{0.5}\text{La}_{0.10}\text{Mn}_{1.40}\text{O}_4$. This implies that lithium ions colonize tetrahedral sites (8a), while La^{3+} ions only conquer the octahedral (16d) sites to replace both nickel and manganese. Furthermore, diffraction intensities of $\text{Li}_{1.05}\text{Ni}_{0.5}\text{La}_{0.10}\text{Mn}_{1.40}\text{O}_4$ are higher, indicating that substituting La^{3+} ions for partial nickel and manganese ions can improve the crystallinity. The partial substitution of Mn with La has the intrinsic benefit of achieving the necessary composite to achieve advantageous electrochemical characteristics apart from the addition of additional carbon. Ionic conductivity can be somewhat increased by partially doping La with Mn^{3+} , because of its larger radius compared to Li^+ . These predict that $\text{Li}_{1.05}\text{Ni}_{0.5}\text{La}_{0.10}\text{Mn}_{1.40}\text{O}_4$ will have better electrochemical performance.¹⁰

Raman spectroscopy was also accustomed to figuring out the framework of the materials as well as the extent of Ni/Mn ordering present in them. Each spectrum has six primary Raman bands with peaks at about, 160, 218, 402, 435, 490, and 607 cm^{-1} that indicate spinel structural characteristics. Ni–O strains provide the strongest Raman signal at 470 cm^{-1} . The middle-frequency bands at 402 cm^{-1} and 435 cm^{-1} can be attributed to the stretching vibrations of the Li–O bonds in LiO_4 and LiO_6 polyhedral, respectively. This observation shows that the alteration does not affect the underlying spinel structure of samples. The typical Raman spectra of well-granulated LNMO materials are seen in Fig. S4a.† Both bands, located at about 400 and 490 cm^{-1} , are related to the Ni–O stretching mode that exists inside the spinel.¹¹ This mode is attributable to the symmetric Mn–O stretching vibration that occurs within the MnO_6 octahedron. The presence of a peak at a frequency of 490 cm^{-1} without any splits suggests that the phase has the disordered structure of an $Fd\bar{3}m$ type. Fig. S4b† shows that the phase has a disorganized structure of the $Fd\bar{3}m$ ratio of the F_{2g} (2) and A_{1g} peaks at 900°C for the sample Nd doped LNMO.¹² This occurs because the ratio of these peaks increases continuously as the heating temperature rises. It is interesting to notice that the Li–La and Li–Nd phonon peak is not visible in the sample that was calcined for Fig. S4b.† This finding suggests that Nd, La, and other transition metals were successfully

absorbed into the spinel lattice during the process of calcination. The identified peaks at 460 cm^{-1} for the high-temperature sample exhibited a small downward shift in frequency, which is indicative of an increase in the lattice parameter caused. Fig. S4c† shows the usual characterization of La-doped LNMO, which is that it has a cubic tight packing of oxygen atoms, with Mn and Ni filling half of the sites in the octahedral area and lithium occupying an eighth of the sites in the tetrahedral region tetrahedral sites. Lithium also occupies an eighth of the tetrahedral sites. In the octahedral sites, which correspond, respectively, to the $Fd\bar{3}m$ and P_{432} space groups, the Mn and Ni ions might be disordered or organized. Due to calcined at 900°C , the intensity ratio of the F_{2g} (2) peak to the A_{1g} peak progressively develops for $\text{Li}_{1.05}\text{Ni}_{0.5}\text{Nd}_{0.10}\text{Mn}_{1.40}\text{O}_4$. There are a few tiny peaks that are characteristic of organized LNMO in space group P_{432} that may be seen between 160 and 218 cm^{-1} .¹³ However, one more characteristic of the ordered phase does not exist; the peak that ought to split into two peaks at around 600 cm^{-1} does not do so. This suggests that the substance contains both an ordered and a disordered phase at approximately equal levels. Because this material has the least amount of Mn^{3+} and the least amount of Ni/Mn disorder, the Ni/Mn arrangement in its structure is likely to be somewhat orderly. This conclusion was reached as a result of the previously discussed structural analysis. There has also been one documented incidence of the illness progressing through both the ordered and disorderly stages.

The FT-IR spectrum was employed to analyze the spinel materials because of their great sensitivity to cation ordering, and discoveries are shown in Fig. S5.† Fig. S5a, b, and c† depict the peaks at 520, 593, and 716 cm^{-1} for samples.¹⁴ These peaks are characteristic of an ordered P_{432} structure and may be identified by their positions. Additional IR absorption bands are detected, indicating that both materials have the order spinel structure. The Mn–O vibration bands are situated at 716 cm^{-1} and 520 cm^{-1} , and they are assigned to the strong bands. Fig. S5a and b, and c† depict the vibration bands of Ni–O. These vibration bands are assigned to the strong bands at 504 cm^{-1} and 593 cm^{-1} .¹⁵ In Fig. S5b† spectrum of $\text{Li}_{1.05}\text{Ni}_{0.5}\text{Nd}_{0.10}\text{Mn}_{1.40}\text{O}_4$, 1215 cm^{-1} is the frequency of the Nd_2O_3 vibration band. Fig. S5c† is a representation of the spectrum of $\text{Li}_{1.05}\text{Ni}_{0.5}\text{La}_{0.10}\text{Mn}_{1.40}\text{O}_4$, in which the vibration bands of La_2O_3 show at 1095 and 1212 cm^{-1} .¹⁶ The intensity of the peaks at 716 cm^{-1} for materials is higher than that at 593 cm^{-1} , which indicates a feature of the $Fd\bar{3}m$ structure. It is therefore possible to deduce that materials have both P_{432} and $Fd\bar{3}m$ phases simultaneously. Both samples are mostly indexed to the P_{432} space group because of the separation of peaks in the 588 to 623 cm^{-1} regions.¹⁷

The produced samples exhibit significant diversity in particle shape and size. As can be seen in Fig. 2a and b, the sample $\text{Li}_{1.05}\text{Ni}_{0.5}\text{Mn}_{1.5}\text{O}_4$ consists mostly of a combination of polyhedral nanoparticles. Fig. 2c and d demonstrate the morphology of the particles of $\text{Li}_{1.05}\text{Ni}_{0.5}\text{Nd}_{0.10}\text{Mn}_{1.40}\text{O}_4$ in which the particles developed further into a truncated octahedral shape with the creation of {100} surfaces.¹⁸ The comparison of these three different materials demonstrates very clearly that



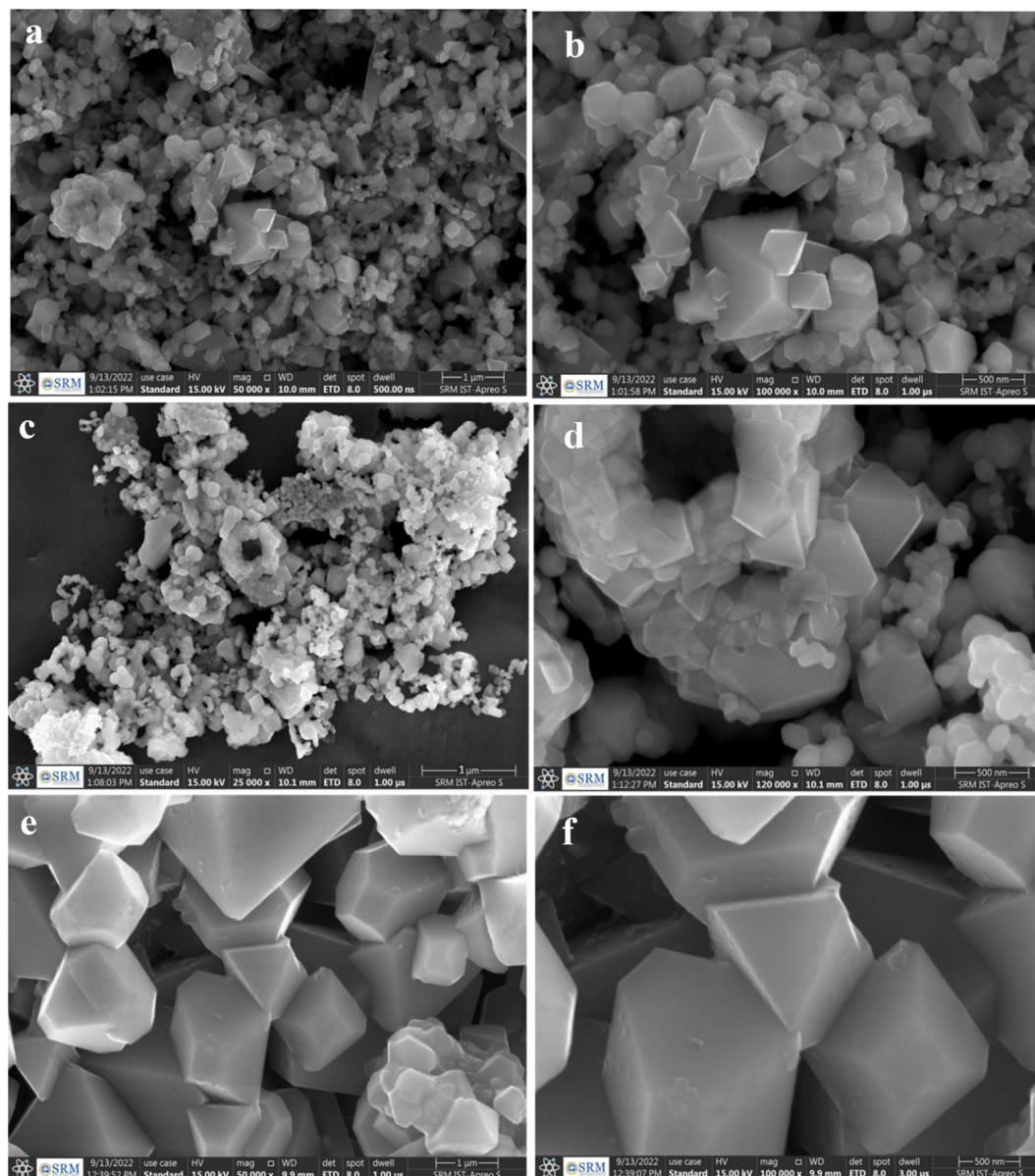


Fig. 2 FE-SEM images of (a, b) $\text{Li}_{1.05}\text{Ni}_{0.5}\text{Mn}_{1.5}\text{O}_4$ (c, d) $\text{Li}_{1.05}\text{Ni}_{0.5}\text{Nd}_{0.10}\text{Mn}_{1.40}\text{O}_4$ and (e, f) $\text{Li}_{1.05}\text{Ni}_{0.5}\text{La}_{0.10}\text{Mn}_{1.40}\text{O}_4$.

a better polyhedral shape can be formed, and the surfaces with a {100} orientation are preferable to be developed very well owing to the calcination temperature that the particle eventually reached a size of around 500 nm and developed into the classic spinel morphology of an octahedral form.¹⁹ This shape is made of {111} surfaces. The micro-sized dimensions were able to be accomplished after the sintering temperature reached 900 °C, as shown in Fig. 2c. During the calcination process, particles penetrate the $\text{Li}_{1.05}\text{Ni}_{0.5}\text{Mn}_{1.5}\text{O}_4$ crystal lattice. Fig. 2e and f demonstrate the morphology of the particles of $\text{Li}_{1.05}\text{Ni}_{0.5}\text{La}_{0.10}\text{Mn}_{1.40}\text{O}_4$ in which the particles developed further into a truncated octahedral shape.

The HRTEM images in Fig. 3a–f represent that the nanoparticles of $\text{Li}_{1.05}\text{Ni}_{0.5}\text{Mn}_{1.5}\text{O}_4$, $\text{Li}_{1.05}\text{Ni}_{0.5}\text{Nd}_{0.10}\text{Mn}_{1.40}\text{O}_4$, and $\text{Li}_{1.05}\text{Ni}_{0.5}\text{La}_{0.10}\text{Mn}_{1.40}\text{O}_4$ were observed with polyhedral,

triclinic and octahedral morphology respectively.²⁰ In Fig. 4, images 4a, 4c, and 4e present that the nanoparticles of $\text{Li}_{1.05}\text{Ni}_{0.5}\text{Mn}_{1.5}\text{O}_4$, $\text{Li}_{1.05}\text{Ni}_{0.5}\text{Nd}_{0.10}\text{Mn}_{1.40}\text{O}_4$, and $\text{Li}_{1.05}\text{Ni}_{0.5}\text{La}_{0.10}\text{Mn}_{1.40}\text{O}_4$ respectively have been crystallized. Fig. 4b $\text{Li}_{1.05}\text{Ni}_{0.5}\text{Mn}_{1.5}\text{O}_4$, Fig. 4d $\text{Li}_{1.05}\text{Ni}_{0.5}\text{Nd}_{0.10}\text{Mn}_{1.40}\text{O}_4$ and Fig. 4f $\text{Li}_{1.05}\text{Ni}_{0.5}\text{La}_{0.10}\text{Mn}_{1.40}\text{O}_4$ presents that the Selected area electron diffraction pattern.²¹ Fig. 4a presents an interplanar spacing of 0.20 nm, 0.27 nm, and 0.47 nm of an interplanar spacing and lattice spacing of 1.89 Å, 2.66 Å, and 4.59 Å corresponding to the (201), (111), and (002) planes of $\text{Li}_{1.05}\text{Ni}_{0.5}\text{Mn}_{1.5}\text{O}_4$ respectively.²² Fig. 4c shows high-resolution lattice fringes with 0.26 nm, 0.45 nm, 0.20 nm, and 0.25 nm of interplanar spacing and lattice spacing of 2.55 Å, 2.47 Å, 2.04 Å and 1.25 Å indicative of the (011), (001), (111), and (021) lattice planes of $\text{Li}_{1.05}\text{Ni}_{0.5}\text{Nd}_{0.10}\text{Mn}_{1.40}\text{O}_4$.²³ Fig. 4d shows the



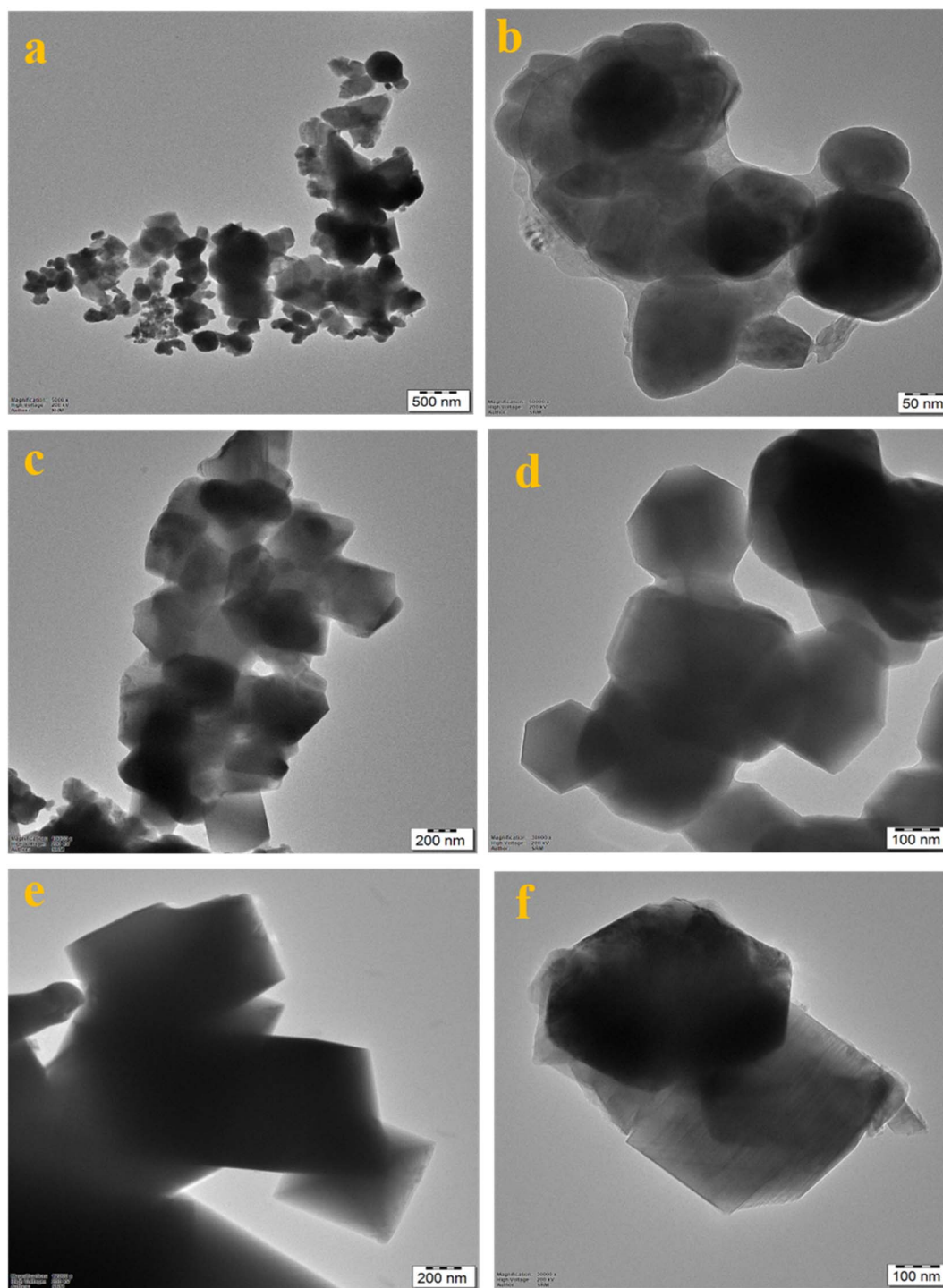


Fig. 3 HR-TEM images of (a, b) $\text{Li}_{1.05}\text{Ni}_{0.5}\text{Mn}_{1.5}\text{O}_4$, (c, d) $\text{Li}_{1.05}\text{Ni}_{0.5}\text{Nd}_{0.10}\text{Mn}_{1.40}\text{O}_4$ and (e, f) $\text{Li}_{1.05}\text{Ni}_{0.5}\text{La}_{0.10}\text{Mn}_{1.40}\text{O}_4$.

distinguished fringe pattern with 0.23 nm, 0.24 nm, and 0.27 nm of interplanar spacing and the lattice spacing of 2.75 Å, 1.93 Å, and 1.37 Å, indexed to the (111), (002), (110) planes of $\text{Li}_{1.05}\text{Ni}_{0.5}\text{La}_{0.10}\text{Mn}_{1.40}\text{O}_4$.²⁴ There seems to be a slight increase in interplanar spacing, which is probably due to the expansion of the lattice units because of an increase in the calcination temperature. The SAED pattern in Fig. 4b shows the crystalline diffraction arrangement corresponding to the (201), (111), (002)

planes of the $\text{Li}_{1.05}\text{Ni}_{0.5}\text{Mn}_{1.5}\text{O}_4$, and the ring radius is calculated with the XRD pattern.²⁵ Fig. 4d shows the crystalline diffraction arrangement corresponding to the (111), (011), (001), and (021) planes of the $\text{Li}_{1.05}\text{Ni}_{0.5}\text{Nd}_{0.10}\text{Mn}_{1.40}\text{O}_4$ and the ring radius is calculated with the XRD pattern.²⁶ Fig. 4f shows the crystalline diffraction arrangement corresponding to the (110), (002), and (111) planes of the $\text{Li}_{1.05}\text{Ni}_{0.5}\text{La}_{0.10}\text{Mn}_{1.40}\text{O}_4$ and the ring radius is calculated with the XRD pattern.²⁷ Fig. S6†



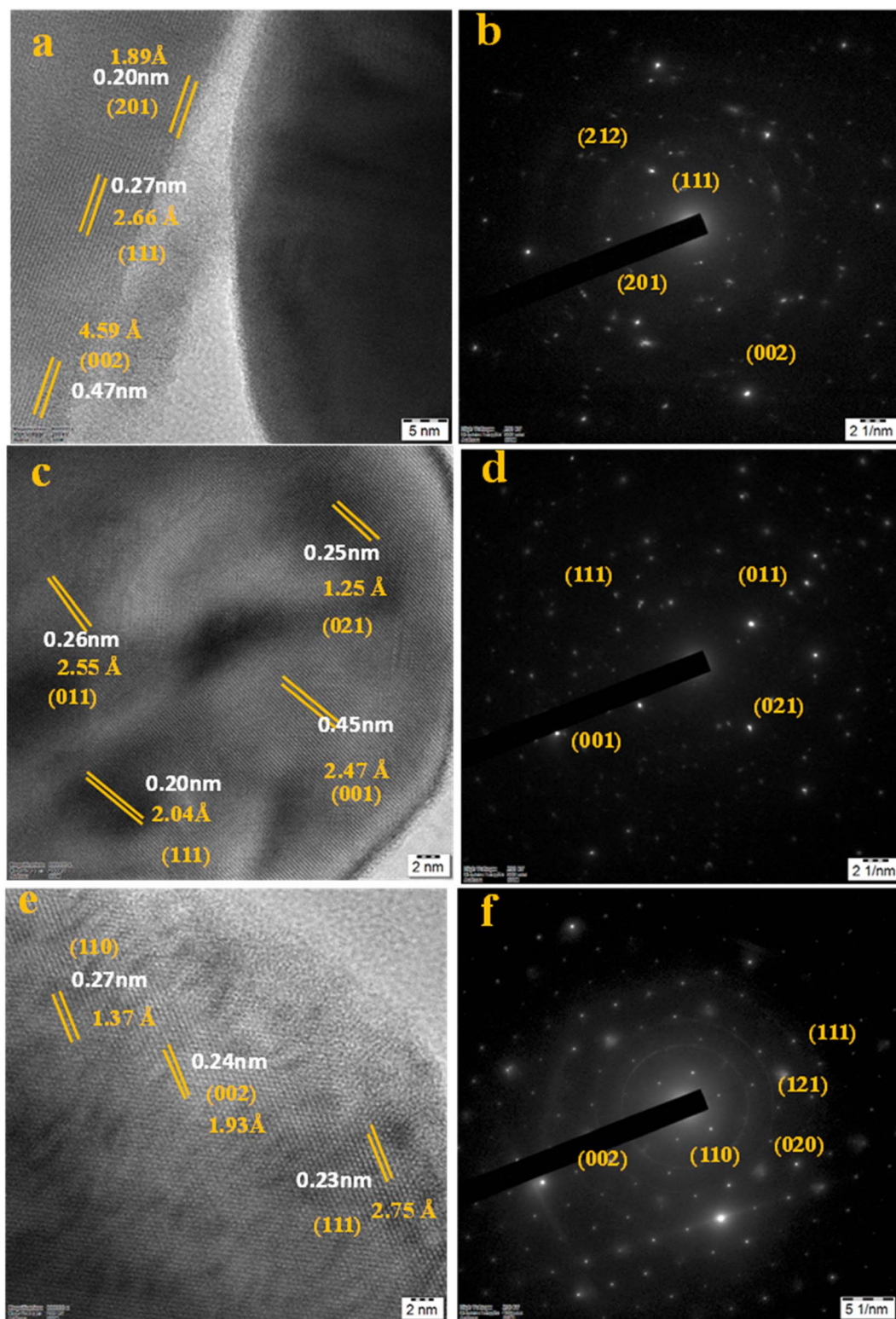


Fig. 4 (a, c, and e) Represent the Lattice spacing of $\text{Li}_{1.05}\text{Ni}_{0.5}\text{Mn}_{1.5}\text{O}_4$, $\text{Li}_{1.05}\text{Ni}_{0.5}\text{Nd}_{0.10}\text{Mn}_{1.40}\text{O}_4$, and $\text{Li}_{1.05}\text{Ni}_{0.5}\text{La}_{0.10}\text{Mn}_{1.40}\text{O}_4$; (b, d, and f) represent selected area electron diffraction pattern of $\text{Li}_{1.05}\text{Ni}_{0.5}\text{Mn}_{1.5}\text{O}_4$, $\text{Li}_{1.05}\text{Ni}_{0.5}\text{Nd}_{0.10}\text{Mn}_{1.40}\text{O}_4$, and $\text{Li}_{1.05}\text{Ni}_{0.5}\text{La}_{0.10}\text{Mn}_{1.40}\text{O}_4$.

represents elemental mapping images of (S6a–S6d†) $\text{Li}_{1.05}\text{Ni}_{0.5}\text{Mn}_{1.5}\text{O}_4$, (S6e–S6i†) $\text{Li}_{1.05}\text{Ni}_{0.5}\text{Nd}_{0.10}\text{Mn}_{1.40}\text{O}_4$ and (S6j–S6n†) $\text{Li}_{1.05}\text{Ni}_{0.5}\text{La}_{0.10}\text{Mn}_{1.40}\text{O}_4$ with a special reference to the

cumulative elemental mapping of the individual particles shows that they have a uniform distribution of O, Mn, Ni, La, Nd, and C in their compositions. The EDX analysis (Fig. S7†)



was performed to validate the constituents found in the prepared $\text{Li}_{1.05}\text{Ni}_{0.5}\text{Mn}_{1.5}\text{O}_4$, $\text{Li}_{1.05}\text{Ni}_{0.5}\text{Nd}_{0.10}\text{Mn}_{1.40}\text{O}_4$, and $\text{Li}_{1.05}\text{Ni}_{0.5}\text{Nd}_{0.10}\text{Mn}_{1.40}\text{O}_4$.

XPS was used to analyze the composition of the as-synthesized materials. The XPS spectrum of $\text{Li}_{1.05}\text{Ni}_{0.5}\text{Mn}_{1.5}\text{O}_4$, $\text{Li}_{1.05}\text{Ni}_{0.5}\text{Nd}_{0.10}\text{Mn}_{1.40}\text{O}_4$, and $\text{Li}_{1.05}\text{Ni}_{0.5}\text{La}_{0.10}\text{Mn}_{1.40}\text{O}_4$, were shown in Fig. S11, S12,† and 5 respectively. In Fig. S11,† during the calcination process, particles penetrate the $\text{Li}_{1.05}\text{Ni}_{0.5}\text{Mn}_{1.5}\text{O}_4$ crystal lattice. To adhere to the principle, the state of Mn ions is changed from oxidation state 4+ to 3+. As a result, the binding energy of Mn2p in all Mn ions must be determined to a higher degree of accuracy.²⁸ Two binding energies in the Mn2p spectrum positioned at 643.49 eV and 654.94 eV in Fig. S11(d)† are often attributed to Mn2p_{1/2} and 2p_{3/2}, with each peak to be further fitted into MnO_2 and Mn_2O_3 line-based peaks that are separate, demonstrating the Mn^{3+} and Mn^{4+} may exist side by side. Mn^{3+} % levels in samples are greater than pristine, demonstrating the transition from after being modified by the calcination step, Mn^{4+} becomes Mn^{3+} . The Mn^{3+} percentages of the samples are demonstrating the transition from Mn^{4+} to Mn^{3+} following calcination at the high-temperature transformation. The binding energies at roughly 851.86 eV, 855.83 eV, 862.88 eV, and 873.40 eV in the XPS spectrum match the Ni2p_{3/2} peaks of $\text{Ni}^{2+}/\text{Ni}^{3+}$ in Fig. S11(c).† An in-depth analysis of the correlation between electrochemical performance and Mn^{3+} concentration reveals that Li requires a high enough level of Mn^{3+} , rate capability, and transport inside the crystalline lattice. Ni ions tend to be concentrated on the surface, and the surface's Ni concentration is larger than the theoretical value.²⁹ In Fig. S12,† The binding energies at 857.22 eV and 863.75 eV in the spectrum of Ni2p (Fig. S12(c)†). Energies involved in the binding process at roughly 874.93 eV and 882.33 eV in the spectrum match the Ni2p_{3/2} peaks of $\text{Ni}^{2+}/\text{Ni}^{3+}$, suggesting that Ni^{2+} and Ni^{3+} coexist in the samples. Peaks around 532.76 eV and 522.73 eV in the O1p XPS spectra (Fig. S12(f)†) are indexed as lattice and oxygen vacancy,

respectively. $\text{Mn}^{3+}/\text{Mn}^{4+}$ are represented by the two peaks with binding energies of 645.16 eV and 656.56 eV, respectively, in Fig. S12(d).† The binding energies at 975.84 eV, 982.94 eV, 996.02 eV, and 1024.31 eV the XPS spectrum of Nd3d (Fig. S12(e)†). The stronger Nd–O bond gives $\text{Li}_{1.05}\text{Ni}_{0.5}\text{Nd}_{0.10}\text{Mn}_{1.40}\text{O}_4$, a higher binding force to oxygen, which helps to prevent irreversible oxygen release and the formation of oxygen vacancies. In Fig. 5, according to electronegativity theory, there is a large difference between the electronegativity of lanthanum and Ni and Mn due to the lower electronegativity of lanthanum, it will “compete” with these two transition metals when forming bonds with oxygen atoms with high electronegativity. The attractiveness of oxygen to the outer layer of a transition metal will be indirectly reduced following La^{3+} doping, which might lead to an increase $\text{Ni}^{2+}/\text{Ni}^{3+}$ ratio. Not only has the $\text{Mn}^{3+}/\text{Mn}^{4+}$ concentration remained constant, but the $\text{Ni}^{2+}/\text{Ni}^{3+}$ ratio has reduced. This might be connected to the reduced oxygen escape following La^{3+} doping. $\text{Li}_{1.05}\text{Ni}_{0.5}\text{La}_{0.10}\text{Mn}_{1.40}\text{O}_4$ includes more lattice oxygen than $\text{Li}_{1.05}\text{Ni}_{0.5}\text{Mn}_{1.5}\text{O}_4$, which weakens and enhances the attraction of electrons to the outer layer of Ni with more oxygen, resulting in La–Li–O having a lower $\text{Ni}^{2+}/\text{Ni}^{3+}$ ratio than LNMO. The two sets of double peaks at 855.42 eV, 851.62 eV, and 838.29 eV, 835.17 eV, which are reported in Fig. 5e, demonstrate the existence of La^{3+} . The binding energies at roughly 851.68 eV and 855.55 eV in the XPS spectrum of Ni2p (Fig. 5c). The binding energies at roughly 862.12 eV and 873.20 eV in the XPS spectrum match the Ni2p_{3/2} peaks of $\text{Ni}^{2+}/\text{Ni}^{3+}$ in Fig. 5c, suggesting that Ni^{2+} and Ni^{3+} coexist in the samples. Furthermore, the peak area ratio of Ni^{2+} and Ni^{3+} can be derived from Fig. 5c, the ion radius of Ni^{2+} is comparable to Li^+ , which will enter the location of Li^+ and result in incomplete embedded or extruded of Li^+ . Because of the combined impact of charge and ion radius, most Li/Ni mixing occurs between Li^+ and Ni^{2+} .³⁰ As a result, the reduced Ni^{2+} concentration of $\text{Li}_{1.05}\text{Ni}_{0.5}\text{La}_{0.10}\text{Mn}_{1.40}\text{O}_4$ is advantageous in reducing Li/Ni mixing, which is congruent with the conclusion

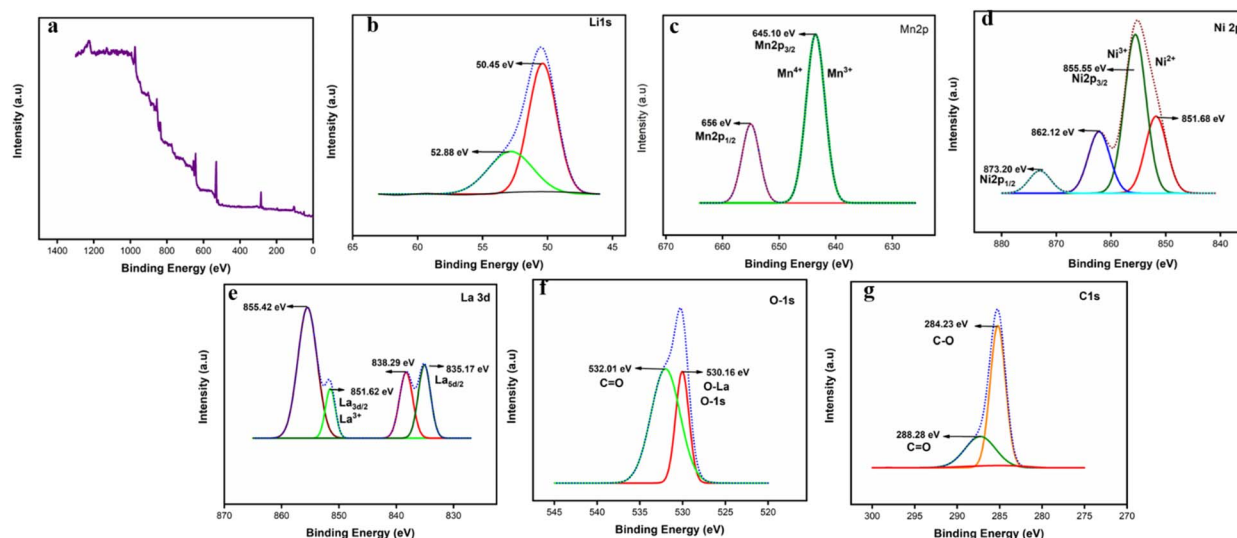


Fig. 5 XPS spectra (a) XPS full survey spectra of $\text{Li}_{1.05}\text{Ni}_{0.5}\text{La}_{0.10}\text{Mn}_{1.40}\text{O}_4$, (b) Li1s, (c) Ni2p, (d) Mn2p, (e) La3d, (f) O1s, (g) C1s.



drawn from XRD patterns. Peaks around 530.16 eV and 532.01 eV in the O1p XPS spectra (Fig. 5f) are indexed as lattice oxygen (O–Mn–O) and oxygen vacancy, respectively. The oxygen vacancy will encourage transition metal ion migration and damage the structure from the surface to the bulk. The stronger La–O bond gives $\text{Li}_{1.05}\text{Ni}_{0.5}\text{La}_{0.10}\text{Mn}_{1.40}\text{O}_4$ a higher binding force to oxygen, which helps to prevent irreversible oxygen release and the formation of oxygen vacancies.³¹ $\text{Mn}^{3+}/\text{Mn}^{4+}$ are represented by the two peaks with binding energies of 645.10 eV and 656 eV, respectively, in Fig. 5d.

4. Electrocatalytic activity performance evaluation

4.1 Hydrogen evolution reaction (HER)

All electrochemical measurements were carried out in 1 M KOH solution at room temperature with platinum (Pt) wire as a counter and Ag/AgCl as a reference electrode.³² Finally, the electrode potentials were converted with respect to a reversible hydrogen electrode (RHE). The working electrode was prepared by, a 4 mg catalyst dissolved in 1 mL solution containing 200 mL IPA, 796 mL DI water, and 4 mL Nafion (5 wt% Sigma-Aldrich) followed by ultrasonication for 45 min in a water bath. First, the glassy carbon (GC) electrode was polished by using 0.5 micron alumina powder.³³ Then 4 mL of this catalyst ink was coated on cleaned glassy carbon (GC) electrode surface (having a geometric surface area of 0.0707 cm^2).³⁴

The synthesized sample of $\text{Li}_{0.5}\text{Ni}_{0.5}\text{Mn}_{1.5}\text{O}_4$, $\text{Li}_{0.5}\text{Ni}_{0.5}\text{La}_{0.10}\text{Mn}_{1.40}\text{O}_4$, and $\text{Li}_{0.5}\text{Ni}_{0.5}\text{Nd}_{0.10}\text{Mn}_{1.40}\text{O}_4$ was evaluated for HER analysis using 1 M KOH as an electrolyte solution and the obtained results are presented in Fig. 6a. The HER activity of $\text{Li}_{0.5}\text{Ni}_{0.5}\text{Mn}_{1.5}\text{O}_4$, and $\text{Li}_{0.5}\text{Ni}_{0.5}\text{Nd}_{0.10}\text{Mn}_{1.40}\text{O}_4$ showed onset potentials at -0.322 V and -0.048 V vs. RHE respectively, whereas, $\text{Li}_{0.5}\text{Ni}_{0.5}\text{La}_{0.10}\text{Mn}_{1.40}\text{O}_4$ showed reduced onset potential -0.016 V vs. RHE which is relatively lower than that of the $\text{Li}_{0.5}\text{Ni}_{0.5}\text{Mn}_{1.5}\text{O}_4$, $\text{Li}_{0.5}\text{Ni}_{0.5}\text{La}_{0.10}\text{Mn}_{1.40}\text{O}_4$ samples. The samples $\text{Li}_{0.5}\text{Ni}_{0.5}\text{Mn}_{1.5}\text{O}_4$, $\text{Li}_{0.5}\text{Ni}_{0.5}\text{La}_{0.10}\text{Mn}_{1.40}\text{O}_4$, and $\text{Li}_{0.5}\text{Ni}_{0.5}\text{Nd}_{0.10}\text{Mn}_{1.40}\text{O}_4$ delivered overpotentials of -0.52 V and -0.20 V , -0.41 V vs. RHE respectively at a current density of 10 mA cm^{-2} . Fig. 6b represents the comparison of onset potential (vs. RHE), current density at 10 mA cm^{-2} , and over potential of all synthesized samples. It is confirmed by the Fig. 6b the onset potential, overpotential at 10 mA cm^{-2} of LNM-La shows enhancement of HER performance than the other samples. The Tafel slope of synthesized materials is presented in Fig. 6c. It is confirmed that the LNM-La reveals a relatively lesser Tafel slope value than that of bare LNM and LNM-Nd. The LNM-La shows a Tafel slope of 73 mV dec^{-1} which is considerably lower than that of LNM (171 mV dec^{-1}) and LNM-Nd (77 mV dec^{-1}). These results strongly suggest that the LNM-La nanocomposite effectively activates water reduction kinetics.³⁵ Further, the chronoamperometric analysis was carried out for 10 hours to evaluate the long-time stability. The ternary nanocomposite of the LNM-La electrode maintained a stable HER activity which

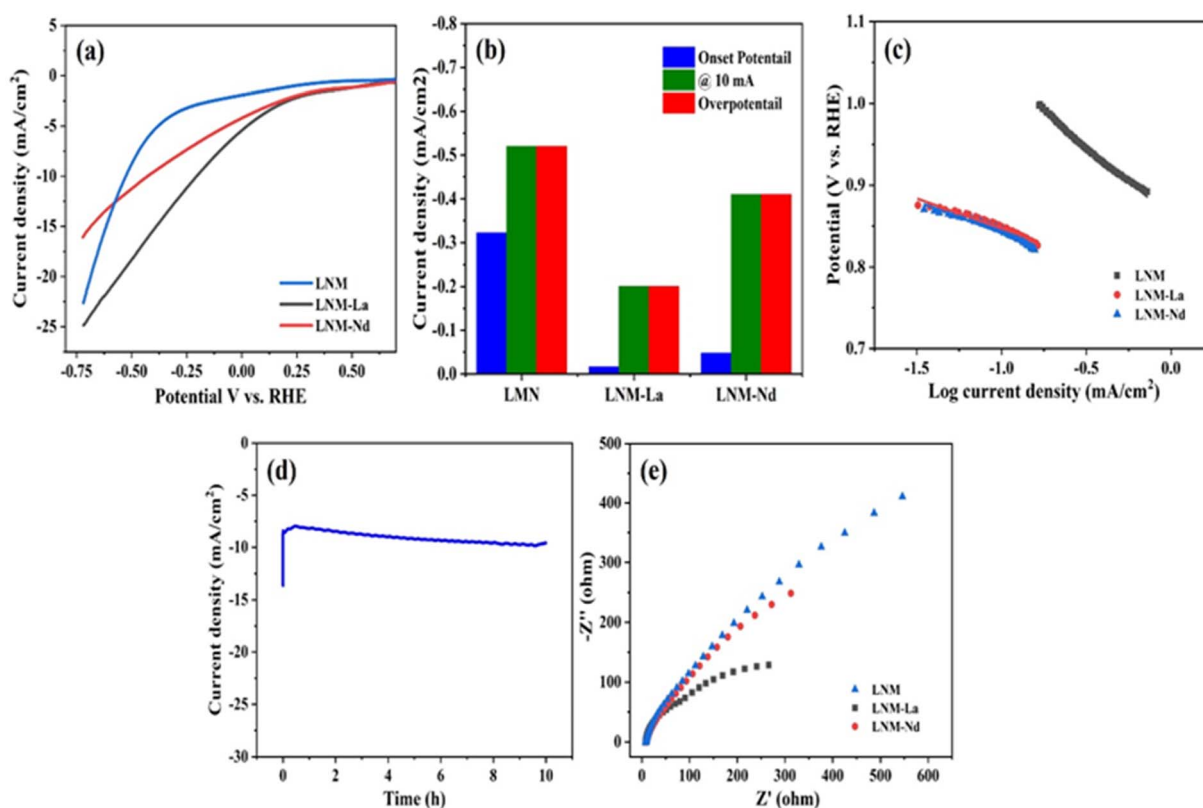


Fig. 6 Electrochemical characterization of synthesized materials in 1 M of KOH electrolyte for HER analysis: (a) polarization curves of LNM, LNM-La, and LNM-Nd; (b) comparison of onset potential, the potential required to reach 10 mA cm^{-2} current density, and overpotential for LNM, LNM-La, and LNM-Nd; (c) corresponding Tafel slopes; (d) stability analysis of LNM-La for HER analysis; (e) EIS analysis of LNM, LNM-La, and LNM-Nd.



gives a constant current at about 10 mA at a potential of 0.20 V vs. RHE (Fig. 6d). Further, the charge transfer resistances of the synthesized electrocatalysis were obtained from the electrochemical impedance spectroscopy (Nyquist plot) in the frequency range of 10 Hz to 100 kHz (Fig. 6e). The charge transfer resistance (R_{ct}) value of LNM, LNM-La, and LNM-Nd reveals 275 ohms, 312 ohms, and 545 ohms respectively. However, the R_{ct} value of LNM-La shows relatively lower when compared with that of LNM, LNM-Nd. The low R_{ct} value will be a favorite for the fast electron transaction hence the LNM-La composite reveals better HER activity than the other samples.³⁶

The enhancement of HER activity of the synthesized nanoparticles was obtained from the electrochemical active surface area (ECSA).³⁷ To obtain the ECSA, the Electrical Double Layer Capacitance (C_{dl}) was identified from the cyclic voltammograms at various scan rates (Fig. S8a–c†). The calculated C_{dl} value of the LNM, LNM-La, and LNM-Nd are $3.78 \mu\text{F cm}^{-2}$, $8.15 \mu\text{F cm}^{-2}$, and $4.14 \mu\text{F cm}^{-2}$ respectively (Fig. S8d†). However, it is observed that the ternary nanocomposite of LNM-La revealed an enhancement of double-layer capacitance and hence enhanced HER activity in the acidic medium.

4.2 Oxygen evolution reaction (OER)

The synthesized sample of $\text{Li}_{0.5}\text{Ni}_{0.5}\text{Mn}_{1.5}\text{O}_4$, $\text{Li}_{0.5}\text{Ni}_{0.5}\text{La}_{0.10}\text{Mn}_{1.40}\text{O}_4$, and $\text{Li}_{0.5}\text{Ni}_{0.5}\text{Nd}_{0.10}\text{Mn}_{1.40}\text{O}_4$ was further evaluated for their OER activities in 1 M KOH electrolyte solution and the obtained results were presented in Fig. 7a. The OER activity of $\text{Li}_{0.5}\text{Ni}_{0.5}\text{Mn}_{1.5}\text{O}_4$ and $\text{Li}_{0.5}\text{Ni}_{0.5}\text{Nd}_{0.10}\text{Mn}_{1.40}\text{O}_4$ showed the onset potentials at 1.8 V and 1.69 V respectively. In contrast,

$\text{Li}_{0.5}\text{Ni}_{0.5}\text{La}_{0.10}\text{Mn}_{1.40}\text{O}_4$ nanocomposite showed considerably low onset potential at 1.69 V vs. RHE. Further, the potential at 10 mA of $\text{Li}_{0.5}\text{Ni}_{0.5}\text{Mn}_{1.5}\text{O}_4$, $\text{Li}_{0.5}\text{Ni}_{0.5}\text{La}_{0.10}\text{Mn}_{1.40}\text{O}_4$, and $\text{Li}_{0.5}\text{Ni}_{0.5}\text{Nd}_{0.10}\text{Mn}_{1.40}\text{O}_4$ synthesized nanoparticles was evaluated and the obtained result is presented in Fig. 7b. The overpotentials obtained for LNM, LNM-Nd, and LNM-La at 10 mA cm^{-2} current density were 2.17 V, 1.93 and 1.68 V vs. RHE respectively. The Tafel plot of the synthesized nanoparticles is presented in Fig. 7c. The Tafel slope values obtained for LNM, LNM-La, and LNM-Nd are 419 mV dec^{-1} , 118 mV dec^{-1} , and 378 mV dec^{-1} respectively. It is observed from Fig. 7c the La-doped LNM revealed a relatively lower slope value when compared with that of LNM, LNM-Nd and other recently reported materials (refer S13†) indicating better water oxidation kinetics of La-doped LNM material.³⁸ Further, the chronoamperometric analysis was carried out for 10 hours to evaluate the long-time stability of the synthesized LNM-La nanocomposite. The LNM-La nanocomposite electrode maintained a stable potential of 1.84 V vs. RHE which gives a constant current at about 12 mA (Fig. 7d). Further, the charge transfer resistance of the synthesized LNM, LNM-La, and LNM-Nd electrocatalysis was obtained from the electrochemical impedance spectroscopy (Nyquist plot) in the frequency range of 10 Hz to 100 kHz (Fig. 7e). The synthesized LNM and LNM-Nd showed relatively high R_{ct} of about 2500 ohms whereas the LNM-La nanocomposites showed a lower R_{ct} resistance of 300 ohms. In the present work, the low R_{ct} value of LNM-La is expected to favor fast electron transfer hence the LNM-La composite revealed better OER as well as HER activity than the other samples. To obtain the ECSA, the Electrical Double Layer Capacitance (C_{dl}) was identified from the cyclic

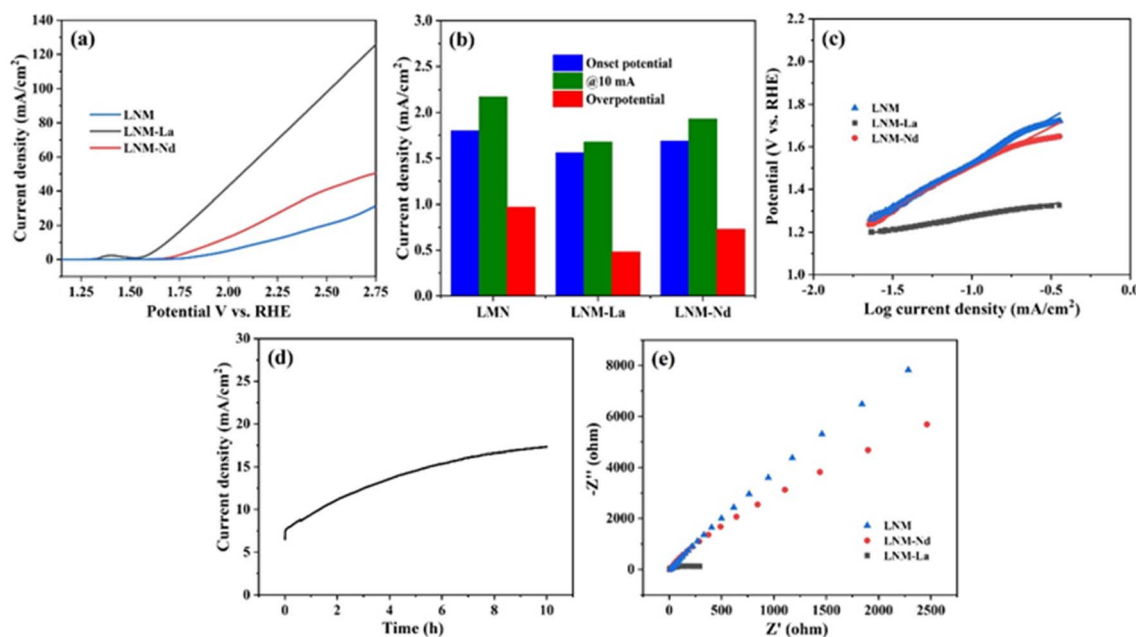


Fig. 7 Electrochemical characterization of synthesized materials in 1 M of KOH electrolyte for OER analysis: (a) polarization curves of LNM, LNM-La, and LNM-Nd; (b) comparison of onset potential, the potential required to reach 10 mA cm^{-2} current density, and overpotential for LNM, LNM-La, and LNM-Nd; (c) corresponding Tafel slopes; (d) stability analysis of LNM-La for OER analysis; (e) EIS analysis of LNM, LNM-La, and LNM-Nd.

voltammograms at various scan rates (Fig. S9a–c†). The calculated C_{dl} values were presented in Fig. S9d† which reveals $2.17 \mu\text{F cm}^{-2}$, $3.56 \mu\text{F cm}^{-2}$, and $2.24 \mu\text{F cm}^{-2}$ for LNM, LNM-La, and LNM-Nd respectively. However, it is observed that the LNM-La nanocomposite reveals enhancement of double-layer capacitance thereby effectively enhancing the OER activity in the alkaline medium. As per the literature, for OER and HER, RuO showed a potential of 1.575 V. and the Pt/C electrode attained an overpotential (η_{10}) of 27 mV, favorable catalytic activity with an onset overpotential (η_{onset}) nearly zero as expected.³⁹ And Tafel plots of RuO₂ for OER and HER are 108 mV dec^{-1} and 170 mV dec^{-1} .⁴⁰ These observed results are compared with freshly prepared electrocatalyst LNM-La showed good OER activity with an overpotential of about 1.68 mV and -0.41 mV , respectively. And Tafel slope of 118 mV dec^{-1} and 73 mV dec^{-1} for OER and HER respectively. As per the literature, for OER and HER, RuO₂ showed a potential of 1.575 V. and the Pt/C electrode attained an overpotential (η_{10}) of 27 mV, favorable catalytic activity with an onset overpotential (η_{onset}) nearly zero as expected.³⁹ And Tafel plots of RuO₂ for OER and HER are 108 mV dec^{-1} and 170 mV dec^{-1} .⁴⁰ These observed results are compared with freshly prepared electrocatalyst LNM-La showed good OER activity with an overpotential of about 1.68 mV and -0.41 mV , respectively. And Tafel slope of 118 mV dec^{-1} and 73 mV dec^{-1} for OER and HER respectively. A prolonged CV for 1000 cycles at a scan rate of 50 mV s^{-1} was used to assess the stability of the $\text{Li}_{1.05}\text{Ni}_{0.5}\text{La}_{0.10}\text{Mn}_{1.40}\text{O}_4$ catalyst. In Fig. S10,† for 1000 cycles, there is a slight change in the shape of the CV curve, it denotes the substantial change in the surface of the electrode as the reaction is carried out, and the mechanism involved here is the adsorbate evolving mechanism (AEM).

5. Conclusions

The objective of this study was to develop a cost-effective, highly active, and stable electrocatalyst for total water splitting. As a result, LNM, LNM-La, and LNM-Nd were synthesized using the solid-state approach. Different characterization procedures were used to evaluate the structural and morphological information of the generated materials. Both OER and HER were tested in alkaline media, these composites exhibited efficient electrocatalytic behaviour for oxygen evolution reaction (OER) as well as hydrogen evolution reaction (HER). At a current density of 10 mA cm^{-2} , the HER activity of LNM, LNM-La, and LNM-Nd nanocomposites provided an overpotential of -0.52 V and -0.20 V , -0.41 V vs. RHE. The LNM-La has a Tafel slope of 73 mV dec^{-1} , which is significantly lower than the LNM (171 mV dec^{-1}) and LNM-Nd (77 mV dec^{-1}). These findings clearly show that the LNM-La nanocomposite successfully stimulates water reduction kinetics. The OER activity of LNM and LNM-Nd has an onset potential of 1.8 V and 1.69 V vs. RHE, respectively. The LNM and LNM-Nd reveal a current density of around 2.17 V and 1.93 V vs. RHE at 10 mA cm^{-2} , respectively. At 10 mA, LNM-La has a potential of roughly 1.68 V. Tafel slope values for the LNM, LNM-La, and LNM-Nd are around 419 mV dec^{-1} , 118 mV dec^{-1} , and 378 mV dec^{-1} , respectively. When compared to LNM and LNM-Nd, La-doped LNM has a lower slope value. These

findings strongly suggest that the LNM-La nanocomposite effectively promotes water oxidation kinetics.

Data availability

All data generated or analyzed during this study are included in this published article.

Conflicts of interest

The authors declared that there are no conflicts of interest.

Acknowledgements

The authors acknowledge the financial support from the Department of Chemistry, SRM Institute of Science and Technology, Tamil Nadu-603 203, India.

References

- 1 M. Praveen Kumar, G. Murugadoss, R. V. Mangalaraja, P. Arunachalam, M. Rajesh Kumar, U. W. Hartley, S. Salla, J. Rajabathar, Z. A. AlOthman and T. AlTalhi, Design and Development of Defect Rich Titania Nanostructure for Efficient Electrocatalyst for Hydrogen Evolution Reaction in an Acidic Electrolyte, *J. Mater. Res. Technol.*, 2021, **14**, 2739–2750, DOI: [10.1016/j.jmrt.2021.07.119](https://doi.org/10.1016/j.jmrt.2021.07.119).
- 2 P. Kaleeswaran, M. P. Kumar, R. V. Mangalaraja, U. W. Hartley, M. Sasikumar, R. Venugopalan, M. R. Kumar, J. R. Rajabathar, S. G. Peera and G. Murugadoss, Fetio3 Perovskite Nanoparticles for Efficient Electrochemical Water Splitting, *Catalysts*, 2021, **11**(9), 1–9, DOI: [10.3390/catal11091028](https://doi.org/10.3390/catal11091028).
- 3 T. V. Vineesh, M. P. Kumar, C. Takahashi, G. Kalita, S. Alwarappan, D. K. Pattanayak and T. N. Narayanan, Bifunctional Electrocatalytic Activity of Boron-Doped Graphene Derived from Boron Carbide, *Adv. Energy Mater.*, 2015, **5**(17), 1–8, DOI: [10.1002/aenm.201500658](https://doi.org/10.1002/aenm.201500658).
- 4 J. Mao, K. Dai, M. Xuan, G. Shao, R. Qiao, W. Yang, V. S. Battaglia and G. Liu, Effect of Chromium and Niobium Doping on the Morphology and Electrochemical Performance of High-Voltage Spinel $\text{LiNi}_0.5\text{Mn}_{1.5}\text{O}_4$ Cathode Material, *ACS Appl. Mater. Interfaces*, 2016, **8**(14), 9116–9124, DOI: [10.1021/acsami.6b00877](https://doi.org/10.1021/acsami.6b00877).
- 5 M. P. Kumar, P. Murugesan, S. Vivek and S. Ravichandran, NiWO_3 Nanoparticles Grown on Graphitic Carbon Nitride (g-C₃N₄) Supported Toray Carbon as an Efficient Bifunctional Electrocatalyst for Oxygen and Hydrogen Evolution Reactions, *Part. Part. Syst. Charact.*, 2017, **34**(10), 1–10, DOI: [10.1002/ppsc.201700043](https://doi.org/10.1002/ppsc.201700043).
- 6 H. Liu, J. Wang, X. Zhang, D. Zhou, X. Qi, B. Qiu, J. Fang, R. Kloepsch, G. Schumacher, Z. Liu and J. Li, Morphological Evolution of High-Voltage Spinel $\text{LiNi}_0.5\text{Mn}_{1.5}\text{O}_4$ Cathode Materials for Lithium-Ion Batteries: The Critical Effects of Surface Orientations and Particle Size, *ACS Appl. Mater. Interfaces*, 2016, **8**(7), 4661–4675, DOI: [10.1021/acsami.5b11389](https://doi.org/10.1021/acsami.5b11389).



- 7 C. J. Jafta, M. K. Mathe, N. Manyala, W. D. Roos and K. I. Ozoemena, Microwave-Assisted Synthesis of High-Voltage Nanostructured LiMn_{1.5}Ni_{0.5}O₄ Spinel: Tuning the Mn³⁺ Content and Electrochemical Performance, *ACS Appl. Mater. Interfaces*, 2013, **5**(15), 7592–7598, DOI: [10.1021/am401894t](#).
- 8 H. B. Lin, Y. M. Zhang, H. B. Rong, S. W. Mai, J. N. Hu, Y. H. Liao, L. D. Xing, M. Q. Xu, X. P. Li and W. S. Li, Crystallographic Facet- and Size-Controllable Synthesis of Spinel LiNi_{0.5}Mn_{1.5}O₄ with Excellent Cyclic Stability as Cathode of High Voltage Lithium Ion Battery, *J. Mater. Chem.*, 2014, **2**(30), 11987–11995, DOI: [10.1039/c4ta01810a](#).
- 9 S. Nageswaran, M. Keppeler, S. J. Kim and M. Srinivasan, Morphology Controlled Si-Modified LiNi_{0.5}Mn_{1.5}O₄ Microspheres as High-Performance High Voltage Cathode Materials in Lithium Ion Batteries, *J. Power Sources*, 2017, **346**, 89–96, DOI: [10.1016/j.jpowsour.2017.02.013](#).
- 10 L. Li, R. Zhao, D. Pan, S. Yi, L. Gao, G. He, H. Zhao, C. Yu and Y. Bai, Constructing Tri-Functional Modification for Spinel LiNi_{0.5}Mn_{1.5}O₄ via Fast Ion Conductor, *J. Power Sources*, 2020, **450**(January), 1–9, DOI: [10.1016/j.jpowsour.2019.227677](#).
- 11 F. Lian, F. Zhang, L. Yang, L. Ma and Y. Li, Constructing a Heterostructural LiNi_{0.4}Mn_{1.6}O₄– δ Material from Concentration-Gradient Framework to Significantly Improve Its Cycling Performance, *ACS Appl. Mater. Interfaces*, 2017, **9**(18), 15822–15829, DOI: [10.1021/acsami.7b01235](#).
- 12 S. Luo, J. Li, J. Lu, F. Tao, J. Wan, B. Zhang, X. Zhou and C. Hu, High-Performance Aqueous Asymmetric Supercapacitor Based on Hierarchical Wheatear-like LiNi_{0.5}Mn_{1.5}O₄ Cathode and Porous Fe₂O₃ Anode, *Mater. Today Phys.*, 2021, **17**, 100337, DOI: [10.1016/j.mtphys.2020.100337](#).
- 13 S. Zhou, Z. Cui, T. Mei, X. Wang and Y. Qian, Hierarchical Desert-Waves-like LiNi_{0.5}Mn_{1.5}O₄ as Advanced Cathodes with Superior Rate Capability and Cycling Stability, *Mater. Today Energy*, 2019, **14**, 100363, DOI: [10.1016/j.mtener.2019.100363](#).
- 14 M. Kunduraci and G. G. Amatucci, Synthesis and Characterization of Nanostructured 4.7 V Li[Sub x]Mn[Sub 1.5]Ni[Sub 0.5]O[Sub 4] Spinel for High-Power Lithium-Ion Batteries, *J. Electrochem. Soc.*, 2006, **153**(7), A1345, DOI: [10.1149/1.2198110](#).
- 15 A. Manthiram, K. Chemelewski and E. S. Lee, A Perspective on the High-Voltage LiMn_{1.5}Ni_{0.5}O₄ Spinel Cathode for Lithium-Ion Batteries, *Energy Environ. Sci.*, 2014, **7**(4), 1339–1350, DOI: [10.1039/c3ee42981d](#).
- 16 S. Divya, R. Pongilat, T. Kuila, K. Nallathamby, S. K. Srivastava and P. Roy, Spinel-Structured NiCo₂O₄ Nanorods as Energy Efficient Electrode for Supercapacitor and Lithium Ion Battery Applications, *J. Nanosci. Nanotechnol.*, 2016, **16**(9), 9761–9770, DOI: [10.1166/jnn.2016.12682](#).
- 17 P. Kalyani, N. Kalaiselvi and N. G. Renganathan, LiNi_MxV_{1-x}O₄ (M = Co, Mg and Al) Solid Solutions - Prospective Cathode Materials for Rechargeable Lithium Batteries?, *Mater. Chem. Phys.*, 2005, **90**(1), 196–202, DOI: [10.1016/j.matchemphys.2004.10.010](#).
- 18 W. Yan, Y. Liu, S. Guo and T. Jiang, Effect of Defects on Decay of Voltage and Capacity for Li[Li_{0.15}Ni_{0.2}Mn_{0.6}]O₂ Cathode Material, *ACS Appl. Mater. Interfaces*, 2016, **8**(19), 12118–12126, DOI: [10.1021/acsami.6b00763](#).
- 19 J. Zhang, G. Sun, Y. Han, F. Yu, X. Qin, G. Shao and Z. Wang, Boosted Electrochemical Performance of LiNi_{0.5}Mn_{1.5}O₄ via Synergistic Modification of Li⁺-Conductive Li₂ZrO₃ Coating Layer and Superficial Zr-Doping, *Electrochim. Acta*, 2020, **343**, 1–10, DOI: [10.1016/j.electacta.2020.136105](#).
- 20 C. Yin, H. Zhou, Z. Yang and J. Li, Synthesis and Electrochemical Properties of LiNi_{0.5}Mn_{1.5}O₄ for Li-Ion Batteries by the Metal-Organic Framework Method, *ACS Appl. Mater. Interfaces*, 2018, **10**(16), 13624–13634, DOI: [10.1021/acsami.8b02553](#).
- 21 Y. Xue, L. L. Zheng, J. Wang, J. G. Zhou, F. Da Yu, G. J. Zhou and Z. B. Wang, Improving Electrochemical Performance of High-Voltage Spinel LiNi_{0.5}Mn_{1.5}O₄ Cathode by Cobalt Surface Modification, *ACS Appl. Energy Mater.*, 2019, **2**(4), 2982–2989, DOI: [10.1021/acsae.9b00564](#).
- 22 T. Yoon, J. Soon, T. J. Lee, J. H. Ryu and S. M. Oh, Dissolution of Cathode-Electrolyte Interphase Deposited on LiNi_{0.5}Mn_{1.5}O₄ for Lithium-Ion Batteries, *J. Power Sources*, 2021, **503**(April), 230051, DOI: [10.1016/j.jpowsour.2021.230051](#).
- 23 C. Yu, L. Dong, Y. Zhang, K. Du, M. Gao, H. Zhao and Y. Bai, Promoting Electrochemical Performances of LiNi_{0.5}Mn_{1.5}O₄ Cathode via YF₃ Surface Coating, *Solid State Ionics*, 2020, **357**(August), 115464, DOI: [10.1016/j.ssi.2020.115464](#).
- 24 C. Liu, M. Wu, Y. Liu, Z. Lu, Y. Yang, S. Shi and G. Yang, Effect of Ball Milling Conditions on Microstructure and Lithium Storage Properties of LiNi_{0.5}Mn_{1.5}O₄ as Cathode for Lithium-Ion Batteries, *Mater. Res. Bull.*, 2018, **99**(November 2017), 436–443, DOI: [10.1016/j.materresbull.2017.11.048](#).
- 25 J. Chong, S. Xun, X. Song, G. Liu and V. S. Battaglia, Surface Stabilized LiNi_{0.5}Mn_{1.5}O₄ Cathode Materials with High-Rate Capability and Long Cycle Life for Lithium Ion Batteries, *Nano Energy*, 2013, **2**(2), 283–293, DOI: [10.1016/j.nanoen.2012.09.013](#).
- 26 Y. Shu, Y. Xie, W. Yan, S. Meng, D. Sun, Y. Jin and K. He, Synergistic Effect of Surface Plane and Particle Sizes on the Electrochemical Performance of LiNi_{0.5}Mn_{1.5}O₄ Cathode Material via a Facile Calcination Process, *J. Power Sources*, 2019, **433**(April), 226708, DOI: [10.1016/j.jpowsour.2019.226708](#).
- 27 H. Wang, T. A. Tan, P. Yang, M. O. Lai and L. Lu, High-Rate Performances of the Ru-Doped Spinel LiNi_{0.5}Mn_{1.5}O₄: Effects of Doping and Particle Size, *J. Phys. Chem. C*, 2011, **115**(13), 6102–6110, DOI: [10.1021/jp110746w](#).
- 28 H. Kawaura, D. Takamatsu, S. Mori, Y. Orikasa, H. Sugaya, H. Murayama, K. Nakanishi, H. Tanida, Y. Koyama, H. Arai, Y. Uchimoto and Z. Ogumi, High Potential Durability of LiNi_{0.5}Mn_{1.5}O₄ Electrodes Studied by Surface Sensitive X-Ray Absorption Spectroscopy, *J. Power*



- Sources, 2014, 245, 816–821, DOI: [10.1016/j.jpowsour.2013.07.011](https://doi.org/10.1016/j.jpowsour.2013.07.011).
- 29 S. Bhuvaneswari, U. V. Varadaraju, R. Gopalan and R. Prakash, Sc-Doping Induced Cation-Disorder in $\text{LiNi}_{0.5}\text{Mn}_{1.5}\text{O}_4$ Spinel Leading to Improved Electrochemical Performance as Cathode in Lithium Ion Batteries, *Electrochim. Acta*, 2019, 327, 135008, DOI: [10.1016/j.electacta.2019.135008](https://doi.org/10.1016/j.electacta.2019.135008).
 - 30 S. Alagar, C. Karupiah, R. Madhuvelakku, S. Piraman and C. C. Yang, Temperature-Controlled Synthesis of Li-and Mn-Rich $\text{Li}_{1.2}\text{Mn}_{0.54}\text{Ni}_{0.13}\text{Co}_{0.13}\text{O}_2$ Hollow Nano/Sub-Microsphere Electrodes for High-Performance Lithium-Ion Battery, *ACS Omega*, 2019, 4(23), 20285–20296, DOI: [10.1021/acsomega.9b02766](https://doi.org/10.1021/acsomega.9b02766).
 - 31 C. Tan, L. Cui, Y. Li, X. Qin, Y. Li, Q. Pan, F. Zheng, H. Wang and Q. Li, Stabilized Cathode Interphase for Enhancing Electrochemical Performance of $\text{LiNi}_{0.5}\text{Mn}_{1.5}\text{O}_4$ -Based Lithium-Ion Battery via Cis-1,2,3,6-Tetrahydrophthalic Anhydride, *ACS Appl. Mater. Interfaces*, 2021, 13(15), DOI: [10.1021/acsami.1c01979](https://doi.org/10.1021/acsami.1c01979).
 - 32 M. M. Baig, I. H. Gul, R. Ahmad, *et al.*, One-step sonochemical synthesis of NiMn-LDH for supercapacitors and overall water splitting, *J. Mater. Sci.*, 2021, (56), 18636–18649, DOI: [10.1007/s10853-021-06431-x](https://doi.org/10.1007/s10853-021-06431-x).
 - 33 R. Khan, M. T. Mehran, M. M. Baig, B. Sarfraz, S. R. Naqvi, M. B. K. Niazi, M. Z. Khan and A. H. Khoja, 3D hierarchical heterostructured LSTN@NiMn-layered double hydroxide as a bifunctional water splitting electrocatalyst for hydrogen production, *Fuel*, 2021, (0016–2361), 285, DOI: [10.1016/j.fuel.2020.119174](https://doi.org/10.1016/j.fuel.2020.119174).
 - 34 P. Wang, J. Qi, X. Chen, C. Li, W. Li, T. Wang, *et al.*, Three-Dimensional Heterostructured NiCoP@NiMn-Layered Double Hydroxide Arrays Supported on Ni Foam as a Bifunctional Electrocatalyst for Overall Water Splitting, *ACS Appl. Mater. Interfaces*, 2020, 12, 4385–4395, DOI: [10.1021/acsami.9b15208](https://doi.org/10.1021/acsami.9b15208).
 - 35 S. Ramakrishnan, B. Jayaraman, M. Vinothkannan, Ae R. Kim, S. Sengodan and D. J. Yoo, Nitrogen-doped graphene encapsulated FeCoMoS nanoparticles as advanced trifunctional catalyst for water splitting devices and zinc–air batteries, *Appl. Catal. B Environ.*, 2020, 279, 0926–3373, DOI: [10.1016/j.apcatb.2020.119381](https://doi.org/10.1016/j.apcatb.2020.119381).
 - 36 N. Logeshwaran, I. R. Panneerselvam, S. Ramakrishnan, R. S. Kumar, A. R. Kim, Y. Wang and D. J. Yoo, Quasi-hexagonal Platinum Nanodendrites Decorated over CoS₂-N-Doped Reduced Graphene Oxide for Electro-Oxidation of C1-, C2-, and C3-Type Alcohols, *Adv. Sci.*, 2022, 9, 2105344, DOI: [10.1002/adv.202105344](https://doi.org/10.1002/adv.202105344).
 - 37 R. Santhosh Kumar, S. C. Karthikeyan, S. Ramakrishnan, S. Vijayapradeep, A. Rhan Kim, J.-S. Kim and D. Jin Yoo, Anion dependency of spinel type cobalt catalysts for efficient overall water splitting in an acid medium, *Chem. Eng. J.*, 2023, 451, 138471, DOI: [10.1016/j.cej.2022.138471](https://doi.org/10.1016/j.cej.2022.138471).
 - 38 M. Babu Poudel, L. Natarajan, Ae R. Kim, S. C. Karthikeyan, S. Vijayapradeep and D. Yoo, Integrated core-shell assembly of Ni₃S₂ nanowires and CoMoP nanosheets as highly efficient bifunctional electrocatalysts for overall water splitting, *J. Alloys Compd.*, 2023, 960, 0925–8388, DOI: [10.1016/j.jallcom.2023.170678](https://doi.org/10.1016/j.jallcom.2023.170678).
 - 39 S. Pavithra, V. K. Jothi, A. Rajaram, S. Ingavale and A. Natarajan, A Facile Synthesis of a Fusiform-Shaped Three-Dimensional Co/Mn@CNDs-MOF Nanocomposite as an Efficient Electrocatalyst for Oxygen Evolution Reaction in Alkaline Medium, *Energy Fuels*, 2022, 36(12), 6409–6419, DOI: [10.1021/acs.energyfuels.2c00780](https://doi.org/10.1021/acs.energyfuels.2c00780).
 - 40 P. Ganesan, M. Prabu, J. Sanetuntikul and S. Shanmugam, Cobalt sulfide nanoparticles grown on nitrogen and sulfur codoped graphene oxide: an efficient electrocatalyst for oxygen reduction and evolution reactions, *ACS Catal.*, 2015, 5, 3625e37, DOI: [10.1021/acscatal.5b00154](https://doi.org/10.1021/acscatal.5b00154).

